Supporting Information

A low-temperature aqueous Se-based battery with rapid reaction kinetics and unprecedented energy density

Guoqiang Liu,‡[a] Linyu Hu,‡[b] Ying Liu,*[a] Maowen Xu,[c] Jiajun Guo,[a] Haichuan Zhou,[a] Guoliang Ma,[a] He Lin,[d] Zhenhuang Su,[d] Chang Liu,[a] Jiangqi Zhao,[a] Chunlong Dai,*[a] and Zifeng Lin*[a]

[a]School of Materials Science & Engineering, Sichuan University, Chengdu, 610065, China.

[b]College of Physics, Sichuan University, Chengdu 610065, P. R. China.

[c]School of Materials and Energy, Chongqing Key Lab for Advanced Materials and Clean Energies of Technologies, Southwest University, Chongqing 400715, P. R. China.

[d]Shanghai Synchrotron Radiation Facility (SSRF), Shanghai Advanced Research Institute, Chinese Academy of Sciences 239 Zhangheng Road, Shanghai 201204, P. R. China.

‡ The authors contribute to the work equally.

*Corresponding authors: liuying5536@scu.edu.cn (Y.L); chunlongdai@scu.edu.cn (C.D.); linzifeng@scu.edu.cn (Z.L.)

Section A. Materials

All materials, including selenium (Se) (Aladdin, Reagent Grade), $CuSO_4 \cdot 5H_2O$ (Aladdin, 99.9%), Dimethyl sulfoxide (DMSO) (Aladdin, AR), $Cu(ClO_4)_2 \cdot 6H_2O$ (Meryer, Reagent Grade), $Zn(ClO_4)_2 \cdot 6H_2O$ (Meryer, Reagent Grade), copper foil (Suzhou Sinero technology Co., Ltd.), zinc foil (Suzhou Sinero technology Co., Ltd.), stainless steel (Guangdong Canrd New Energy Technology Co., Ltd.), porous carbon (Nanjing Momentum Materials Technologies Co. Ltd.), and anion exchange membrane (AGC-APS, Apsilon technology Co., Ltd.), are used without further purification.

Section B. Experimental section

Preparation of electrolytes. 0.5 m $CuSO_4$ electrolyte was prepared through adding 0.12 g $CuSO_4 \cdot 5\ H_2O$ in 1 g deionized water. 3, 4, 5, 6, 7 m $Cu(ClO_4)_2$ electrolytes were prepared through adding 1.11, 1.48, 1.85, 2.22, 2.59 g $Cu(ClO_4)_2 \cdot 6\ H_2O$ in 1 g deionized water, respectively. 6 m $Zn(ClO_4)_2$ electrolyte was prepared through adding 2.23 g 6 m $Zn(ClO_4)_2$ $6H_2O$ in 1 g deionized water.

Synthesis of Se@C composite. Se@C composites are obtained by melt diffusion strategy. Typically, porous carbon and selenium powder are mixed in the mass ratio of 30:70, and then heated in a tube furnace at 260 °C under an argon atmosphere for 12 h.

Electrode preparation. Se@C cathode electrode (thickness: ~350 μm) was prepared as follows: Se@C, carbon black (Alfa Aesar, 99%), and polyvinylidenefluoride (PVDF) binder (Alfa Aesar) of 8:1:1 mass ratio in the appropriate amount of N-Methyl-2-pyrrolidone (NMP, Aladdin, 99.5%) solvent were milled into a slurry, and then the slurry was uniformly coated on the stainless-steel mesh (8 mm in diameter). The cathode was obtained after dried under vacuum at 60 °C for 12 h. The areal mass loading of Se is 1.5~2 mg cm^{-2}.

Section C. Methods

Material characterizations. The morphology and microstructure analysis of the synthesized materials were examined by scanning electron microscopy (SEM, JSM-7900F) and energy dispersive spectroscopy (EDS, Ultima MAX 65). Operando X-ray diffraction (XRD) tests were conducted on Bruker D8 Advance (Cu-K_α, $\lambda = 0.15406$ nm, 40 kV). Synchrotron XRD measurement of electrodes under different conditions were performed on the BL14B1 beamline at Shanghai Synchrotron Radiation Facility (SSRF), the wavelength of the X-ray is 0.6887 nm. The content of Se in the prepared composite was estimated using Thermogravimetric analysis (TGA, TGA/DSC3+/1600). Differential scanning calorimetry (DSC, Netzsch DSC 200 F3) was used to measure the freezing point of the electrolytes, which was carried out in the procedure of +30 ~ −170 °C with a cooling rate of 10 K min^{-1}, keeping at −170 °C for 5 mins, and then

heating up to +30 °C with a heating rate of 10 K min^{-1}. Fourier transform infrared (FTIR) analysis was recorded on NEXUS 670. Raman spectroscopy of the electrolyte structure was conducted on LabRAM HR with a 532 nm excitation laser. Nuclear magnetic resonance (NMR) analysis was characterized on Bruker ASCEND 400. Lattice and elemental analysis of the electrode samples were carried out by transmission electron microscopy (TEM, JEOL JEM2800F).

Electrochemical measurements. The electrochemical performance of the Cu-Se@C cell was tested in the 2032 coin cell. The Cu-Se@C coin cells were assembled by pairing cathode casing, Se@C cathode (8 mm in diameter), separators (Whatman GF/D, 16 mm in diameter), Cu foil (12 mm in diameter), gaskets, springs and anode casing, where their masses are about 0.88, 0.01, 0.03, 0.01, 1.51, 0.31, 0.86 g respectively, and the total mass of coin cells is about 3.81 g (the amount of electrolyte was 200 μL calendering pressures: 10 MPa). The Zn-Se full cell was investigated in a homemade cell (as shown in Figure S39), where Se@C acted as the cathode, 6 m $Cu(ClO_4)_2$ as the catholyte, 6 m $Zn(ClO_4)_2$ as the anolyte (the amount of electrolytes were all 1 mL), Zn as the anode, and an anion-exchange membrane (2 × 2 cm) was used to separate the catholyte and the anolyte. All low-temperature performance was obtained by testing in two high-low-temperature chambers (−55~110 °C, SG-80-CC-2, Sanwood technology Co., Ltd., −75~150 °C, JL-E702-100B70, Hunan Julang Instrument Co.). The low-temperature electrochemical performance of the batteries was tested by activating them for three cycles at room temperature.

The rate performance, cycling stability, and galvanostatic intermittent titration technique (GITT) measurement of Se-based batteries were conducted by the Neware battery testing system (5 V, 10 mA, Shenzhen, China). **(Note:** all specific capacity or energy density values in the manuscript are calculated based on the mass of Se unless otherwise noted. All polarization voltages in this work were determined by the potential difference between charge and discharge curves at the mid-capacity point of the total discharge specific capacity.**)**The cyclic voltammetry (CV), linear scanning voltammetry (LSV) and the chronoamperometry (CA) were tested by an electrochemical workstation (SP-150e, BioLogic). The electrochemical impedance spectroscopy (EIS) was carried on CHI760E with the frequency from 100 kHz to 0.1 Hz.

The ionic conductivity of aqueous electrolytes is calculated by the following equation (1):

$$\sigma = \frac{L}{R_s \times A} \qquad \text{(Equation 1)}$$

where σ is the ionic conductivity of the electrolyte (mS cm^{-1}), R_s is the electrolyte resistance (Ω), L is the distance between two electrodes (1 cm), A is the area of the electrode (1 cm^2).

The activation energy of aqueous electrolytes in the low temperature range is calculated by the following equation (2) and (3):

$$\sigma = \frac{A}{T} e^{-\frac{E_a}{kT}} \quad \text{(Equation 2)}$$

$$\ln(\sigma T) = \ln(A) - \frac{E_a}{kT} \quad \text{(Equation 3)}$$

where σ is the ionic conductivity of the electrolyte (mS cm^{-1}), T is temperature (K); E_a is activation energy; k is Boltzmann constant (1.380649×10^{-23} J K^{-1}). The $-E_a/k$ was fitted by different temperature ln (σT) and 1/T. The E_a was obtained.

The energy densities were calculated by the following equation:

$$E = \int U \times Q \quad \text{(Equation 4)}$$

where U is the cell operating voltage of discharge, Q is the discharge specific capacity of the cell. The discharge specific capacity is calculated based on mass of Se cathode.

Calculation of the energy density of Zn-Se full cell:

The full cell energy density is calculated based on the total mass of the Se cathode, carbon host of Se, carbon black, binder (PVDF), $Cu(ClO_4)_2$, and Zn anode.

The transference number of Cu^{2+} was tested in Cu||Cu symmetrical cells by EIS before and after the CA tests and calculated by the following equation:

$$T_{Cu^{2+}} = \frac{I_s(\Delta V - I_0 R_0)}{I_0(\Delta V - I_s R_s)} \quad \text{(Equation 5)}$$

where ΔV is the applied voltage polarization, I_s and R_s are the steady state current and resistance, respectively, and I_0 and R_0 are the initial current and resistance, respectively. The applied voltage polarization is 25 mV.

The Cu^{2+} diffusion coefficient is calculated by the following equation (5):

$$D = \frac{4}{\pi\tau}\left(\frac{m_B V_M}{M_B S}\right)^2 \left(\frac{\Delta E_s}{\Delta E_t}\right)^2 \quad \text{(Equation 6)}$$

where D is Cu^{2+} diffusion coefficient; m_B, M_B and V_m are the mass, molecular weight, and molar volume of material (Se); S is the contact area between electrolyte and electrode; τ is the charge or discharge pulses time (300 s); ΔE_S is the change of the steady-state voltage of the cell over a single titration; ΔE_τ is the cell voltage during charging or discharging at the time of current of flux.

Computational Methods. Electrolyte structures were analyzed through molecular dynamics (MD) simulations using the Forcite module in Materials Studio with COMPASS III force field.[1,

[2] The MD simulations were performed in a cubic box (32.7 × 32.7 × 32.7 $Å^3$), and the numbers of water molecules and ions are listed in Table S4. Geometric optimizations were initiated using the COMPASS III force field with ultrafine quality parameters (convergence tolerance of energy: 2.0×10^{-5} kcal mol^{-1}, force tolerance: 1×10^{-3} kcal mol^{-1} $Å^{-1}$, displacement tolerance: 1×10^{-5} Å). Subsequently, NPT (constant particle number, pressure, and temperature) runs were conducted over 5 ns with a timestep of 1.0 fs to ensure system equilibrium. After reaching equilibrium state, another 5 nm simulation under NVT ensemble was performed. The last 2.5 ns of the simulation were utilized for subsequent analysis. The binding energy calculations were performed using Gaussian 16 software within the density functional theory (DFT) framework. All molecular structures were computed using the B3LYP (Becke, three-parameter, Lee–Yang–Parr) hybrid functional, which accounts for the exchange-correlation interactions. For the high-level B3LYP computations, the 6-311++G(d,p) basis set was applied to O, Cl, and H atoms.

Section D. Supplementary Figures

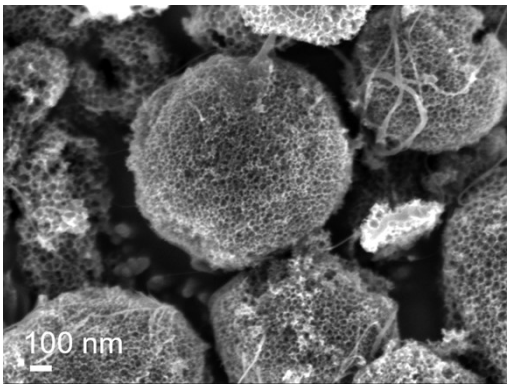

Fig. S1. SEM images of the porous carbon.

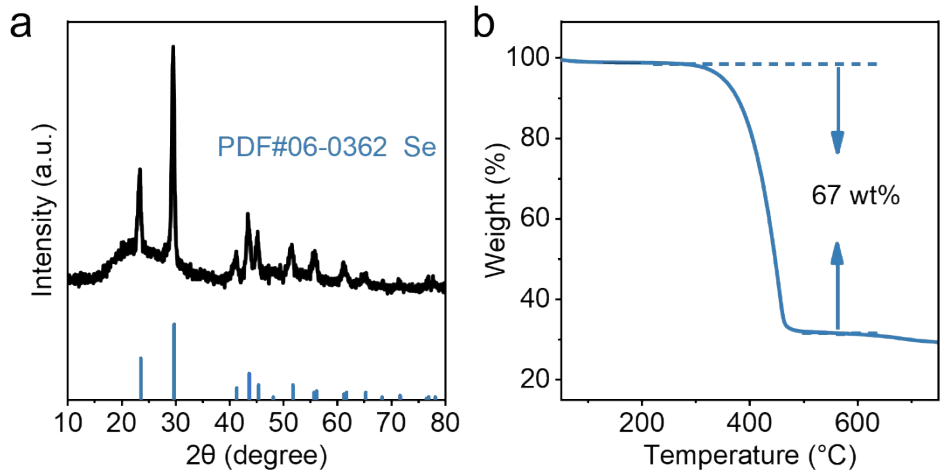

Fig. S2. (a) The XRD pattern of the Se@C composite; (b) The TGA curves of the Se@C composite.

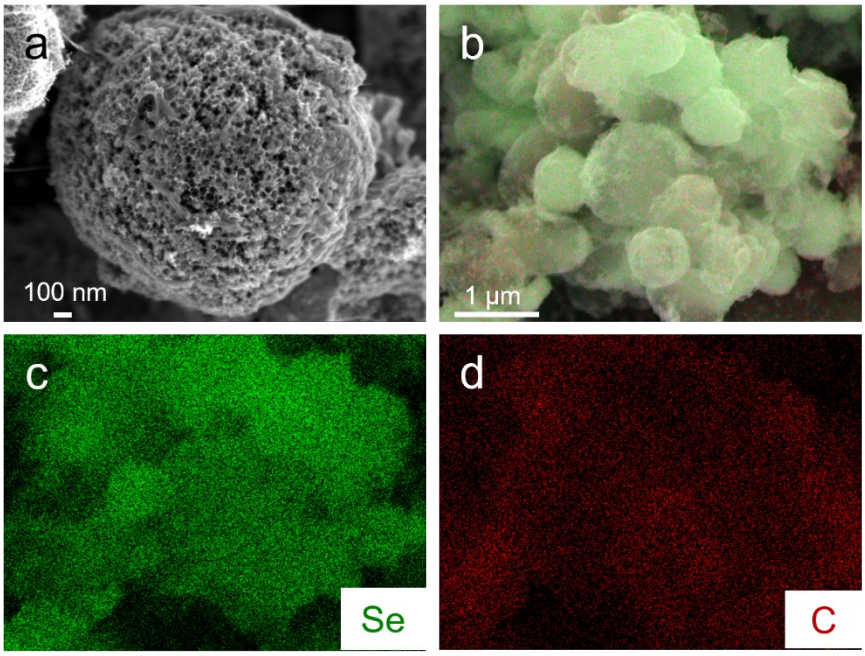

Fig. S3. SEM images, and corresponding element mappings of the Se@C composite.

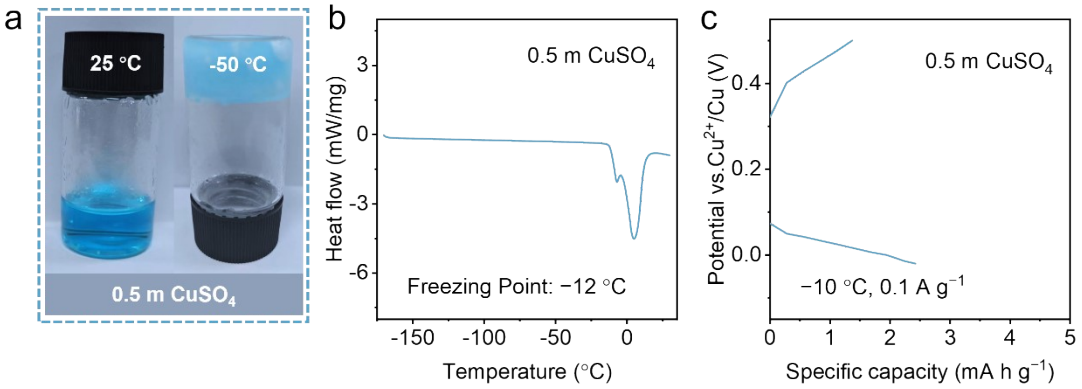

Fig. S4. (a) The optical photograph of 0.5 m $CuSO_4$ at 25 °C and −50 °C; (b) DSC curve of 0.5 m $CuSO_4$; (c) The GCD curve of Cu|0.5m $CuSO_4$|Se@C coin cell at 0.1 A g^{-1} at −10 °C.

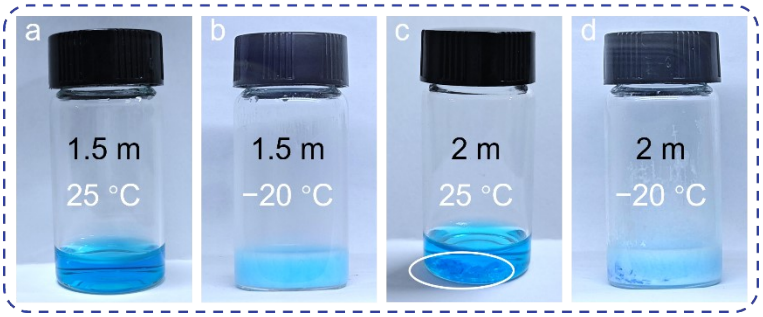

Fig. S5. Optical photographs of 1.5 m $CuSO_4$ aqueous solutions at (a) 25 °C, (b) −20 °C and 2 m $CuSO_4$ aqueous solutions at (c) 25 °C, (d) −20 °C.

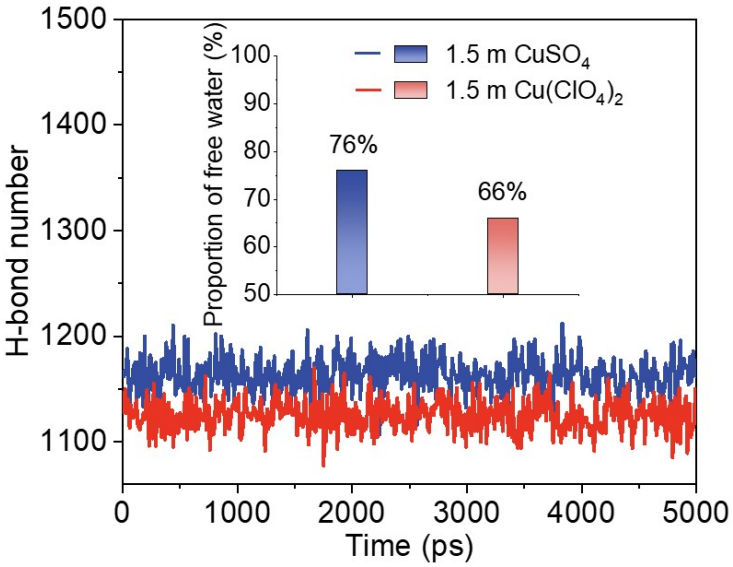

Fig. S6 Comparison of H-bond number and proportion of free water in 1.5 m $CuSO_4$ and 1.5 m $Cu(ClO_4)_2$ electrolytes.

Fig. S7. The optical photograph of 0.5 m $CuSO_4$ in DMSO (DMSO with a molar fraction of 0.3).

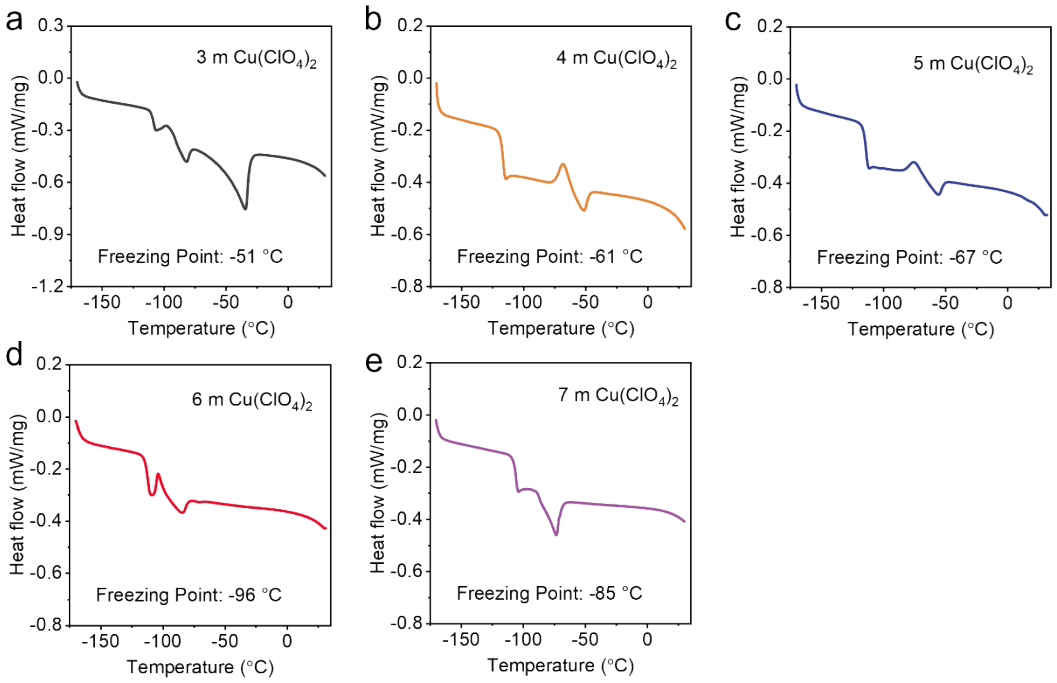

Fig. S8. DSC curves of 3, 4, 5, 6, 7 m $Cu(ClO_4)_2$ electrolytes.

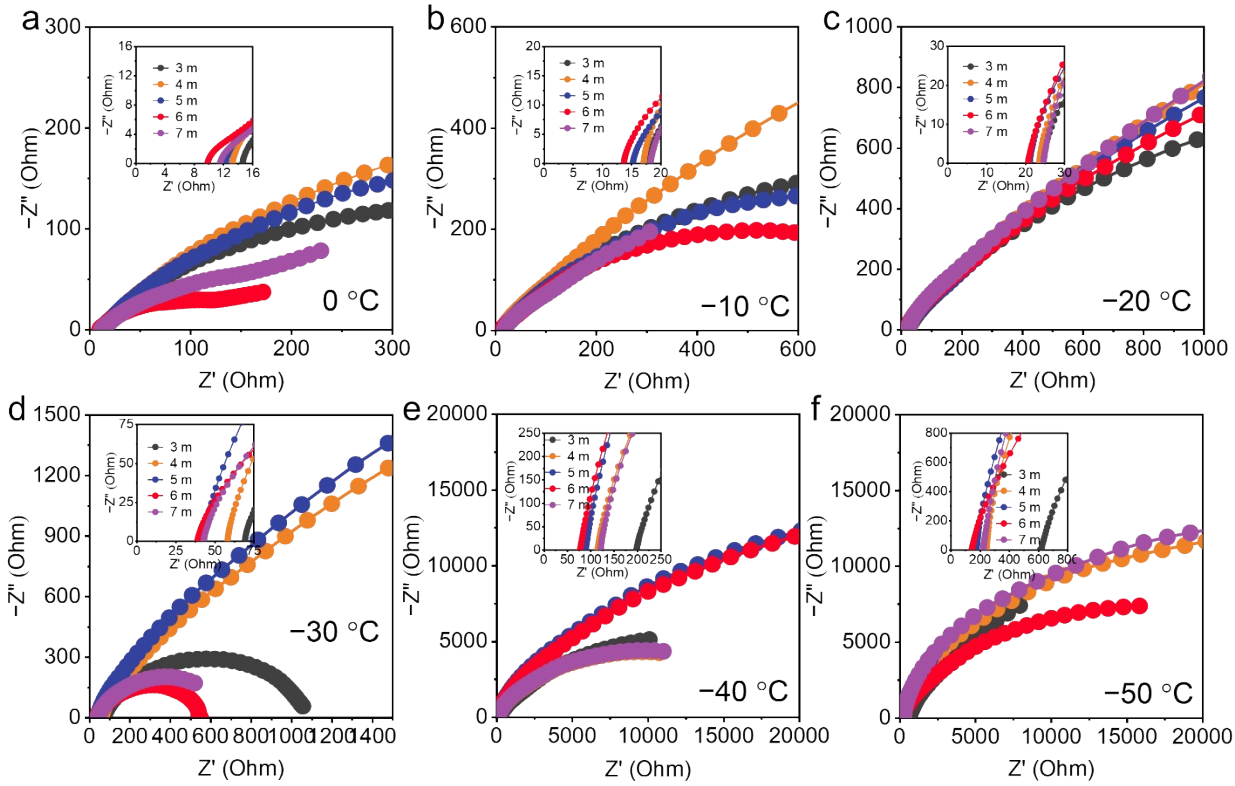

Fig. S9. Nyquist plot of electrochemical impedance spectroscopy (EIS) for 3, 4, 5, 6, 7 m $Cu(ClO_4)_2$ electrolytes at different temperatures.

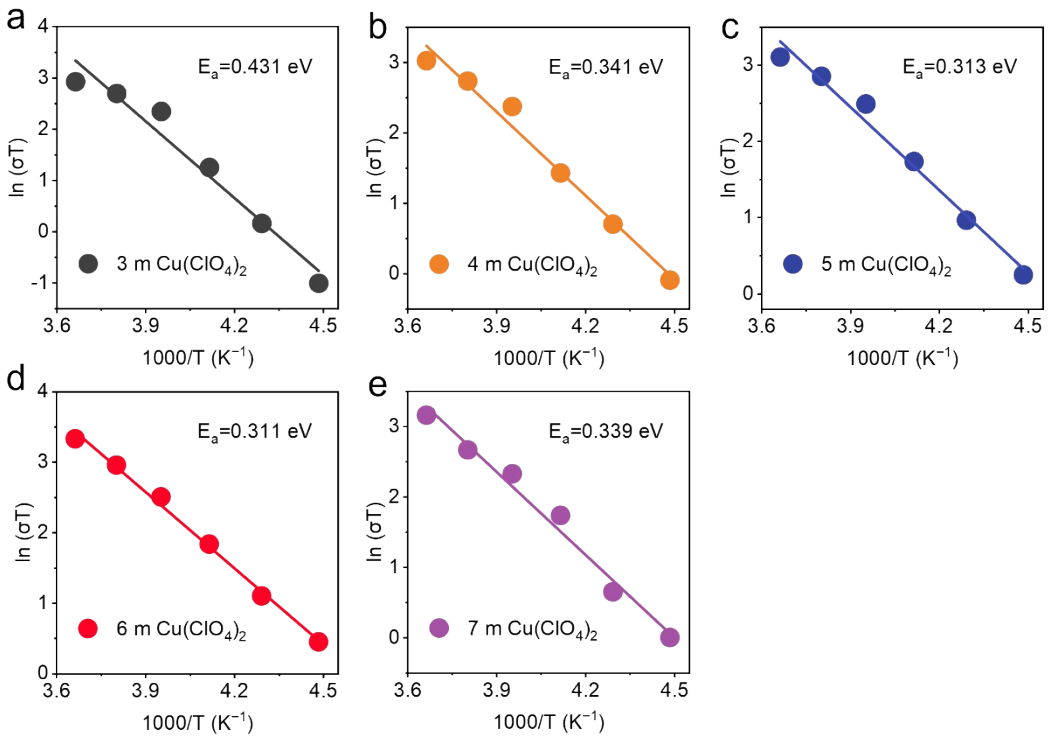

Fig. S10. Electric conductance activation energy of 3, 4, 5, 6, 7 m $Cu(ClO_4)_2$ electrolytes.

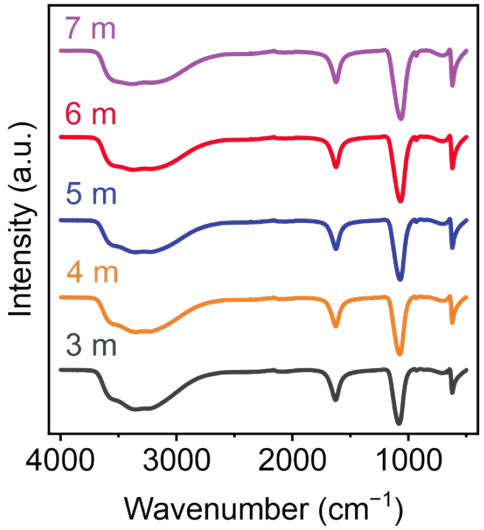

Fig. S11. The FTIR total spectra of 3, 4, 5, 6 and 7 m $Cu(ClO_4)_2$ electrolytes.

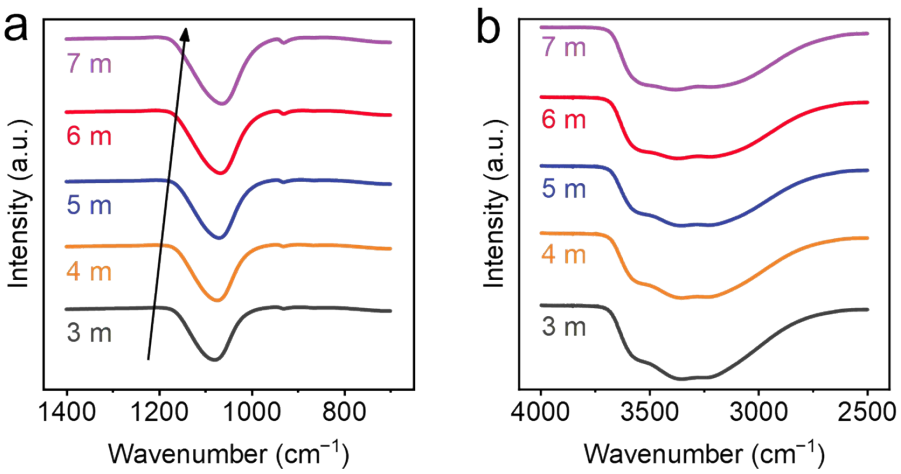

Fig. S12. FTIR spectra for (a) Cl–O bond and (b) O–H bond.

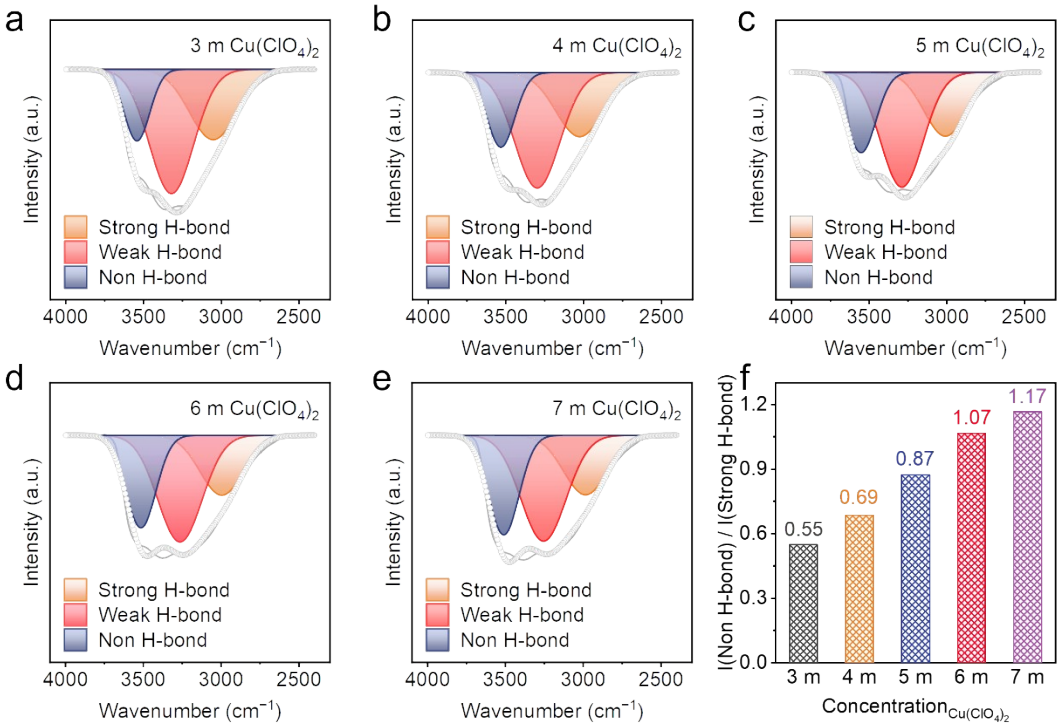

Fig. S13. The fitted O−H stretching vibration of FTIR spectra representing water molecules with strong H-bond, weak H-bond and Non H-bond in the $Cu(ClO_4)_2$ electrolytes with different concentrations. (a) 3 m $Cu(ClO_4)_2$; (b) 4 m $Cu(ClO_4)_2$; (c) 5 m $Cu(ClO_4)_2$; (d) 6 m $Cu(ClO_4)_2$; (e) 7 m $Cu(ClO_4)_2$ (f) The intensity ratio of the non H-bond and strong H-bond vibration bands ($I_{\text{Non H-bond}} / I_{\text{Strong H-bond}}$).

Note: The peak at ~3000 cm^{-1} is ascribed to strong H-bond. And the peak at ~3530 cm^{-1} refers to the non H-bond, which is the result of interaction between water molecules and ClO_4^- anions. These two peak areas are used to calculate the ratio of non H-bond to strong H-bond.

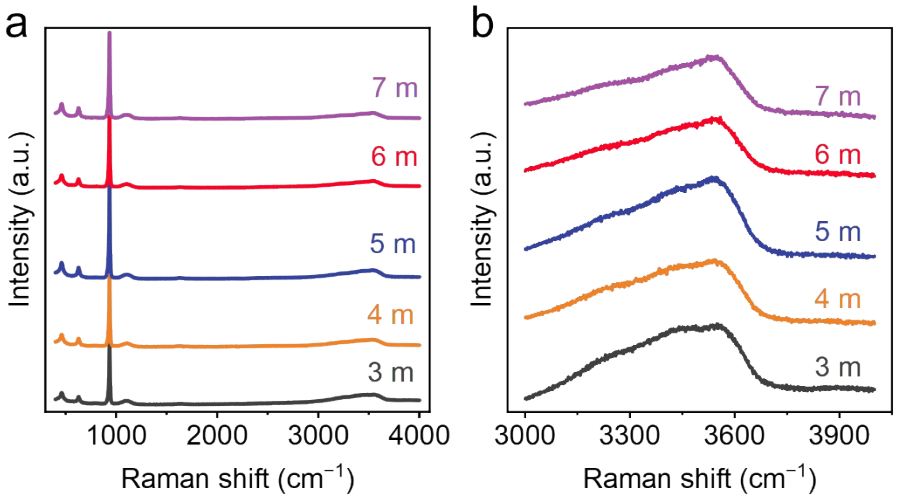

Fig. S14. (a) The all Raman spectra and (b) Raman spectra for O–H bond of 3, 4, 5, 6 and 7 m $Cu(ClO_4)_2$ electrolytes.

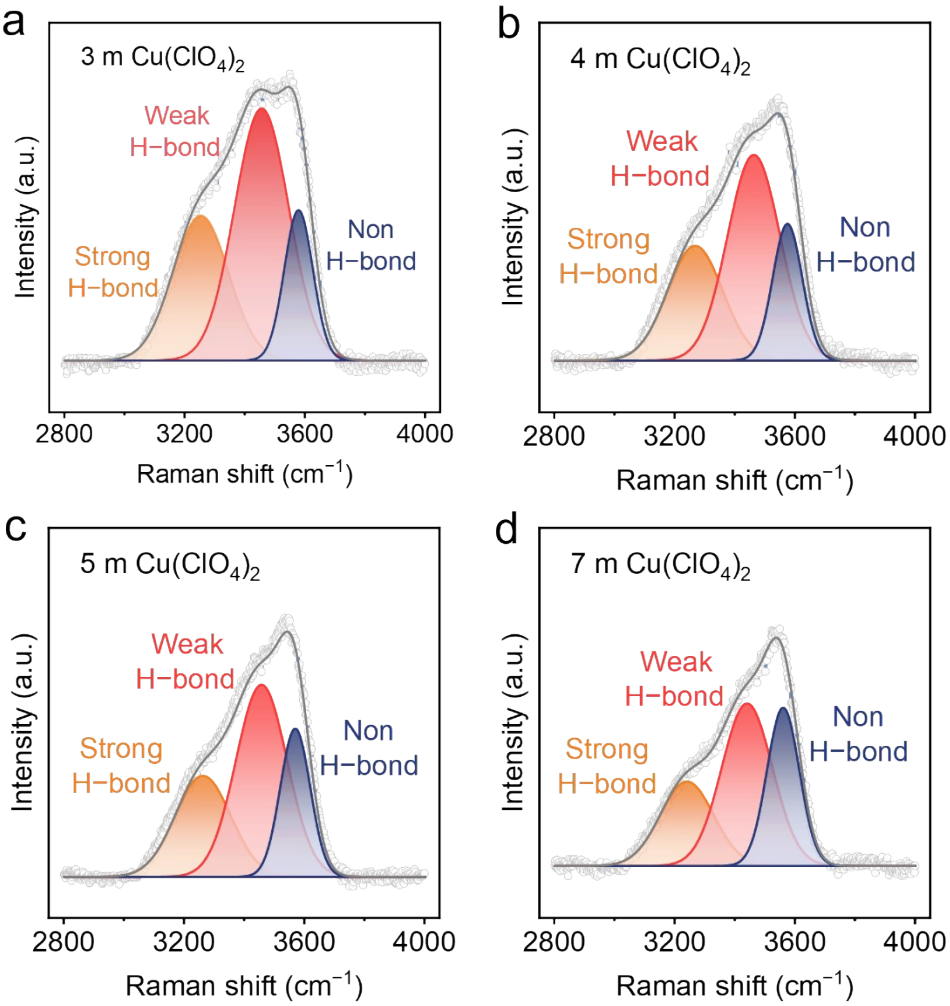

Fig. S15. The fitted O−H stretching vibration of Raman spectra representing water molecules with strong H−bond, weak H−bond, and Non H−bond in the $Cu(ClO_4)_2$ electrolytes with different concentrations. (a) 3 m $Cu(ClO_4)_2$; (b) 4 m $Cu(ClO_4)_2$; (c) 5 m $Cu(ClO_4)_2$; (d) 7 m $Cu(ClO_4)_2$.

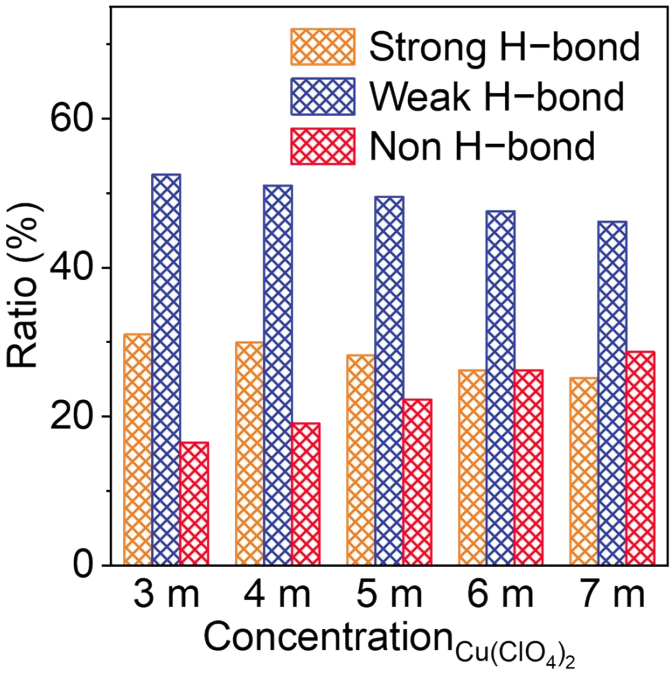

Fig. S16. The proportion of strong H-bond, weak H-bond, and non H-bond in of $Cu(ClO_4)_2$ solutions with different concentrations.

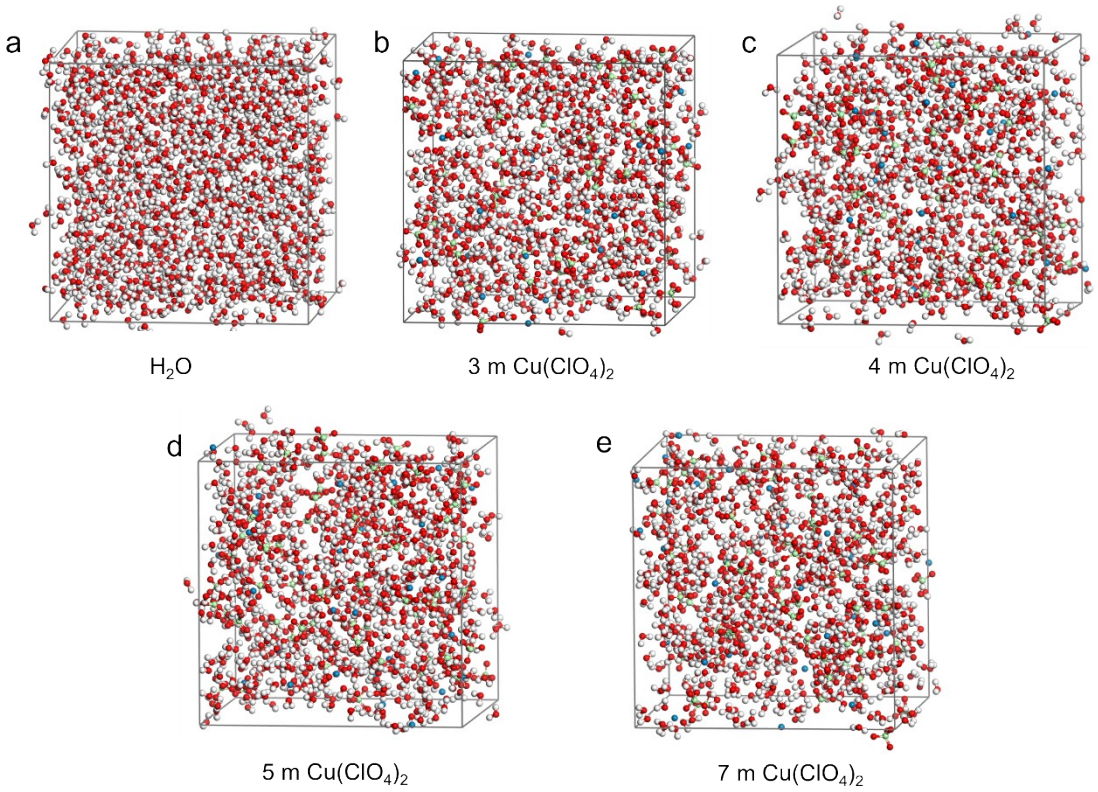

Fig. S17. The 3D snapshot of (A) H_2O, (B) 3 m $Cu(ClO_4)_2$, (C) 4 m $Cu(ClO_4)_2$, (D) 5 m $Cu(ClO_4)_2$, and (E)7 m $Cu(ClO_4)_2$ electrolytes.

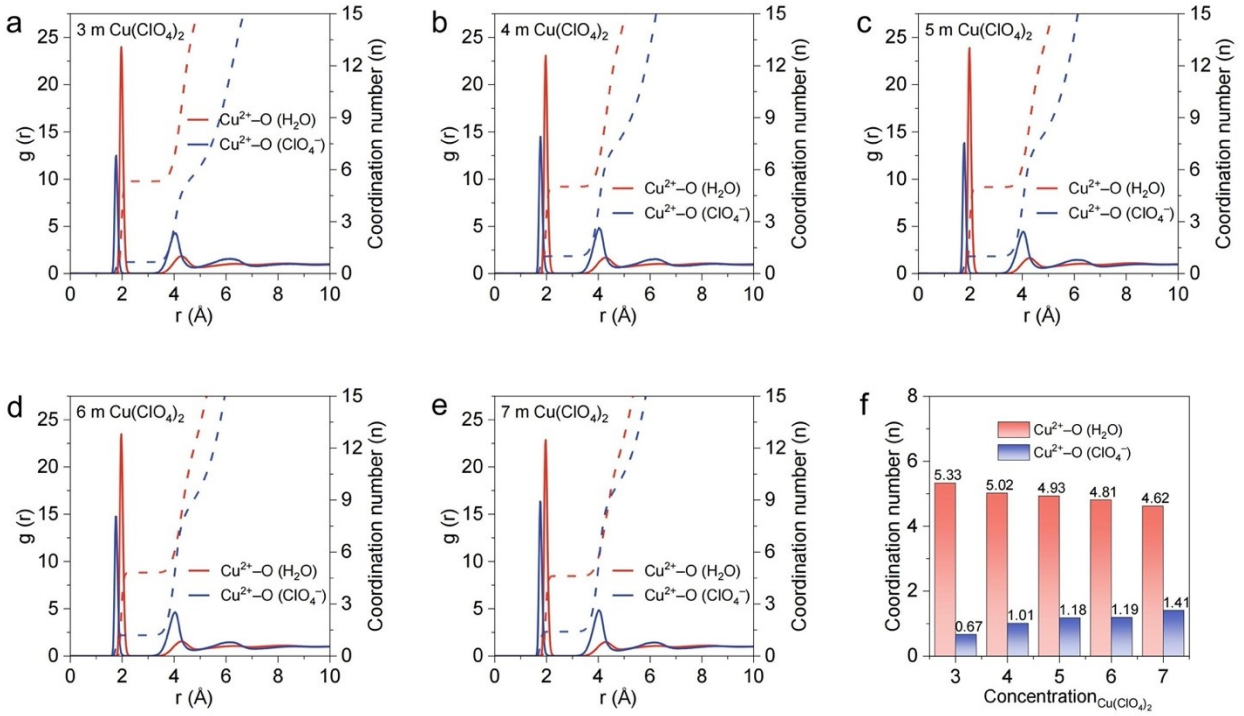

Fig. S18. Radial distribution function (RDF) and coordination numbers of Cu^{2+}-O (H_2O) and Cu^{2+}-O (ClO_4^-) in (a) 3 m, (b) 4 m, (c) 5 m, (d) 6 m and (e) 7 m $Cu(ClO_4)_2$ electrolytes. (f) Comparison of coordination numbers in different concentration of electrolytes.

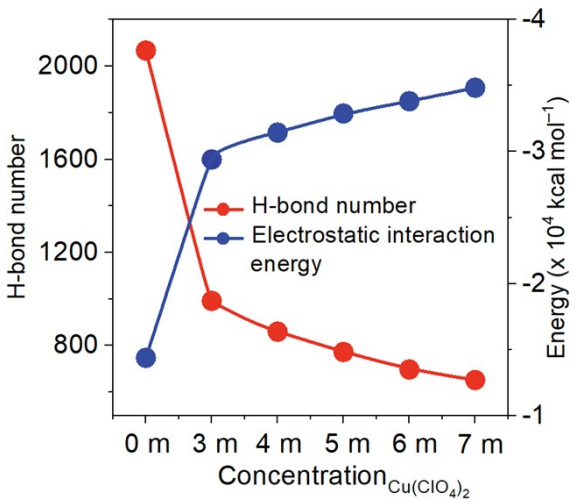

Fig. S19. Comparison of H-bond number and the electrostatic interaction energy of different concentrations of electrolytes.

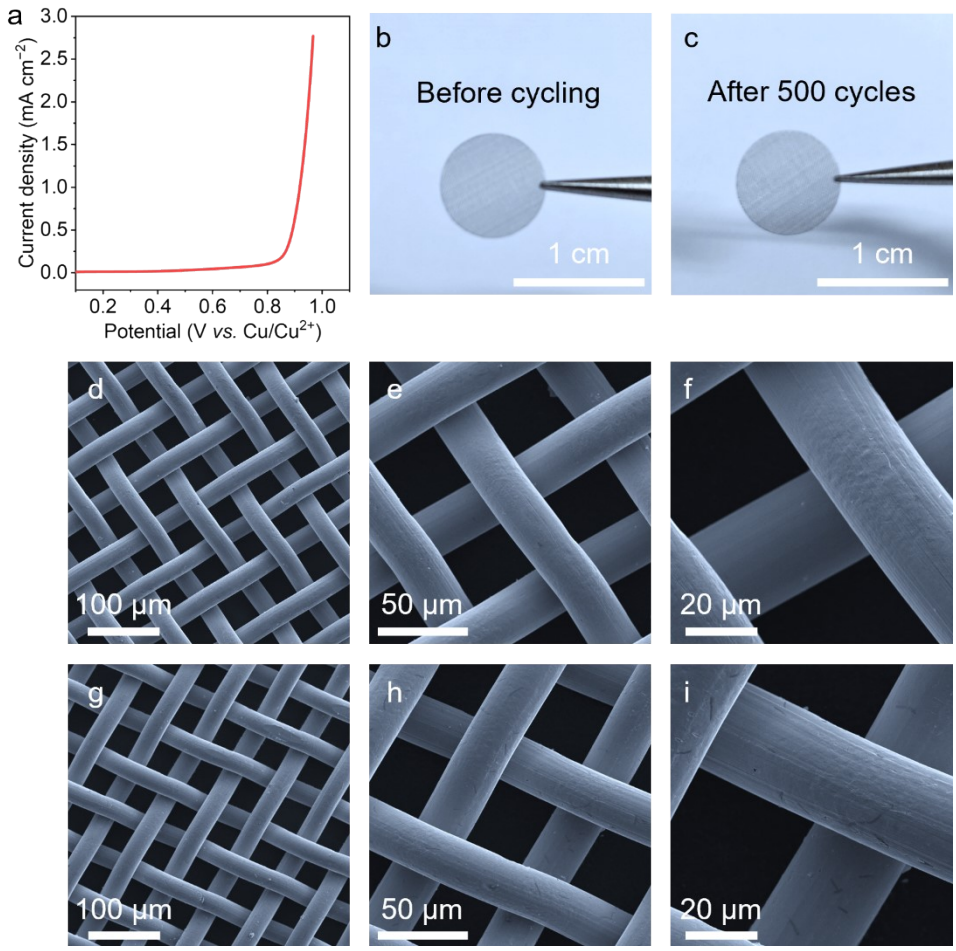

Fig. S20. (a) Oxygen evolution reaction (OER) in 6 m $Cu(ClO_4)_2$ measured using linear potential scan (LSV) at a scan rate of 1 mV s^{-1} in Cu||SS cells; digital photographs and SEM images of SS before (b, d-f) and after (c, g-i) CV test for 500 cycles in Cu//SS cells within 0 ~ 0.5 V.

The stainless steel used as a current collector is 316L grade, which is well known for its excellent corrosion resistance. The Cu||SS (stainless steel) cell in 6 m $Cu(ClO_4)_2$ exhibits an onset potential of about 0.85 V *vs.* Cu/Cu^{2+} (Fig. S20a), which is higher than the maximum test potential of 0.5 V *vs.* Cu/Cu^{2+} for the Cu||Se cell, indicating that there is no reaction occurring and no corrosion effect in the pure stainless steel within the test voltage range of the Cu||Se cell in 6 m $Cu(ClO_4)_2$ electrolyte. Furthermore, SEM and optical images (Fig. S20b-i) reveal no morphological changes in the SS after 500 CV cycles, further indicating that high-concentration perchlorate electrolyte cannot cause corrosion to the stainless steel.

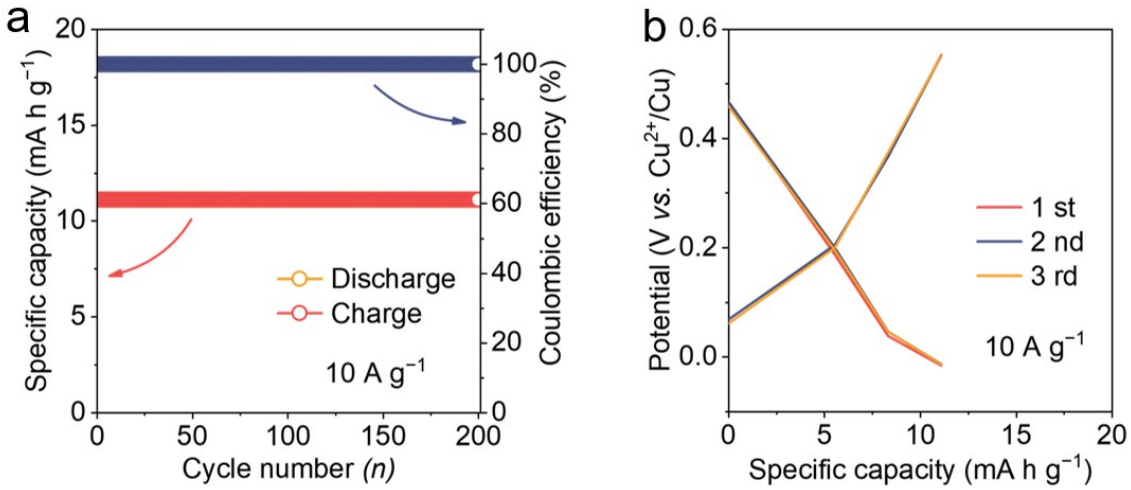

Fig. S21. (a) Cycling stability test, and (b) GCD curves of the Cu|6 m $Cu(ClO_4)_2$|C cells with carbon as the cathode.

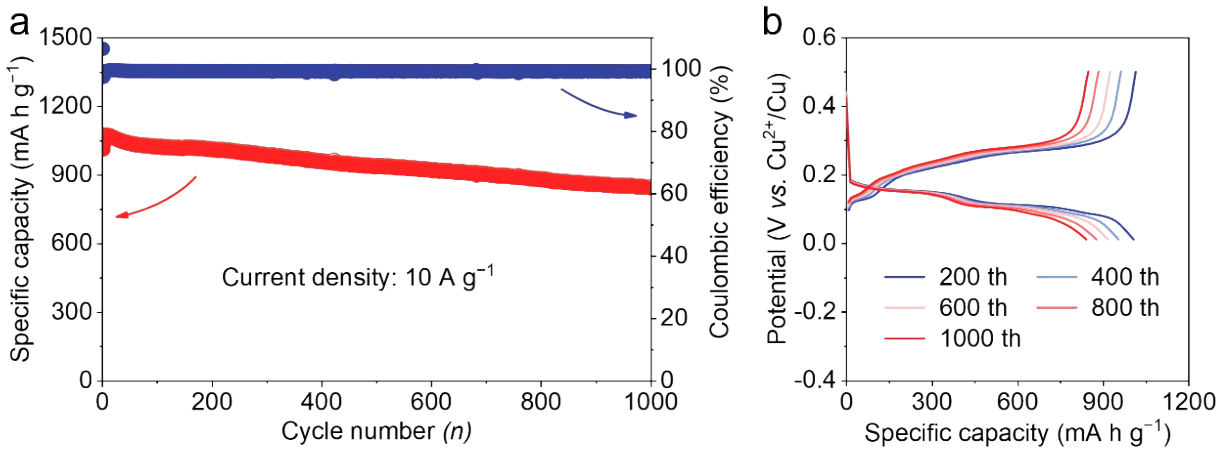

Fig. S22. (a) Cycling stability test, and (b) GCD curves at different cycles of the Cu|6 m $Cu(ClO_4)_2$|Se@C cells.

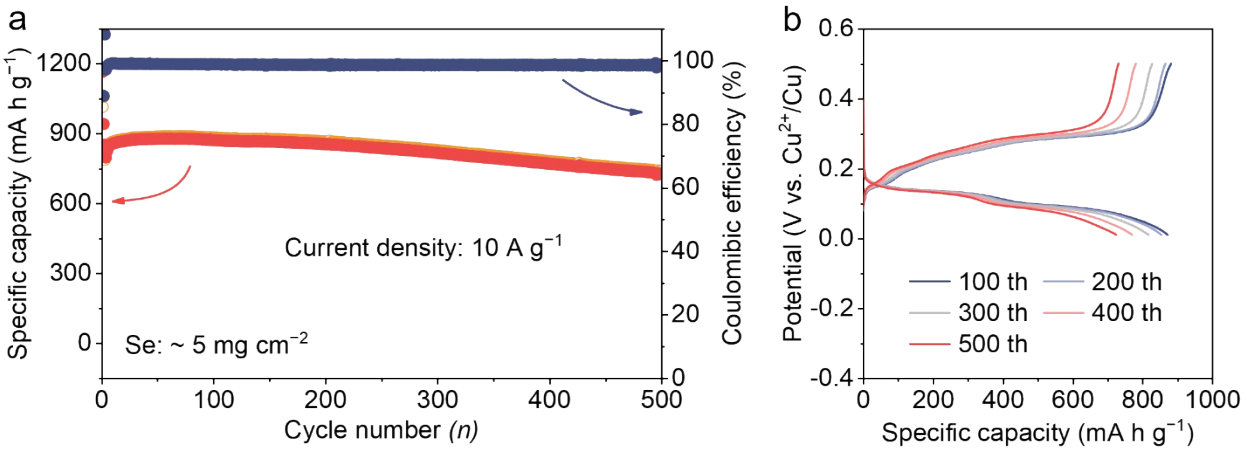

Fig. S23. (a) Cycling stability test, and (b) GCD curves of the Cu|6 m $Cu(ClO_4)_2$|Se@C cells with a higher Se loading of ~ 5 mg cm^{-2} at 10 A g^{-1}.

It also delivers a stable cycling life, maintaining 85% capacity retention based on the first-cycle capacity at 10 A g^{-1} after 500 cycles.

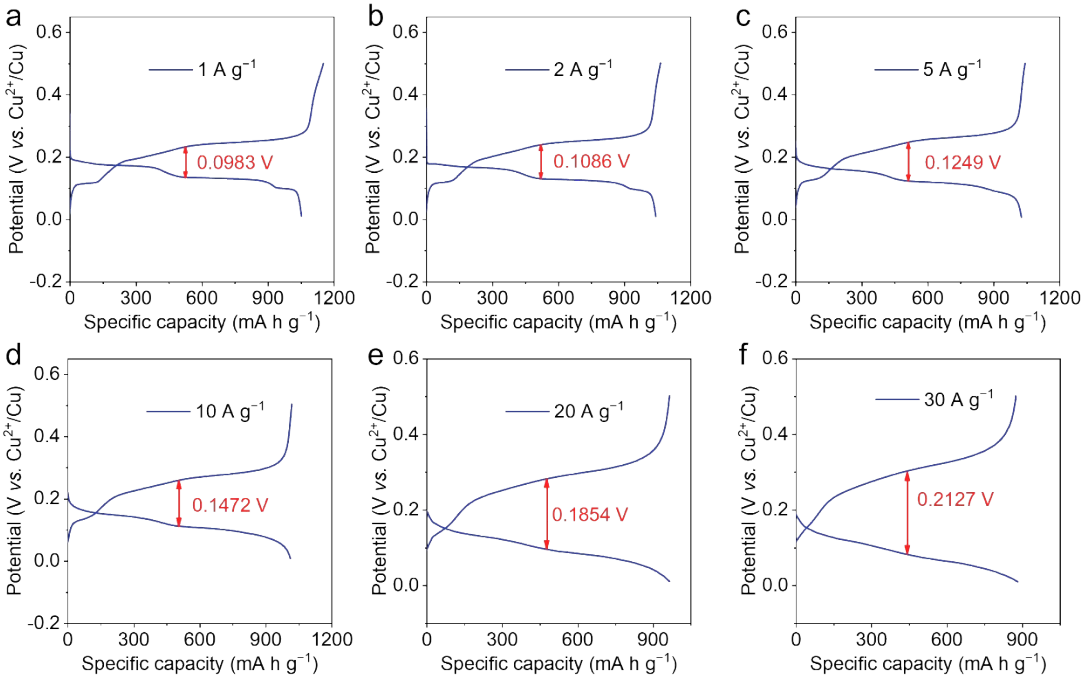

Fig. S24. The polarization between discharging and charging curves of the Cu|6 m $Cu(ClO_4)_2$|Se@C cells at 1, 2, 5, 10, 20, 30 A g^{-1}.

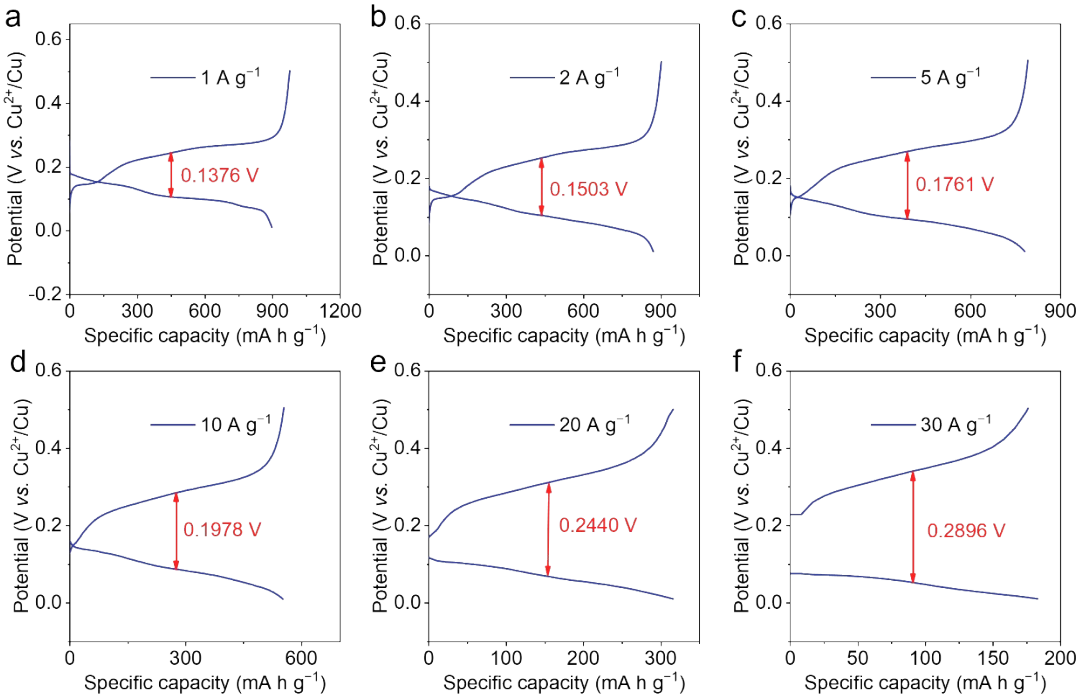

Fig. S25. The polarization between discharging and charging curves of the Cu|0.5 m $CuSO_4$|Se@C cells at 1, 2, 5, 10, 20, 30 A g^{-1}.

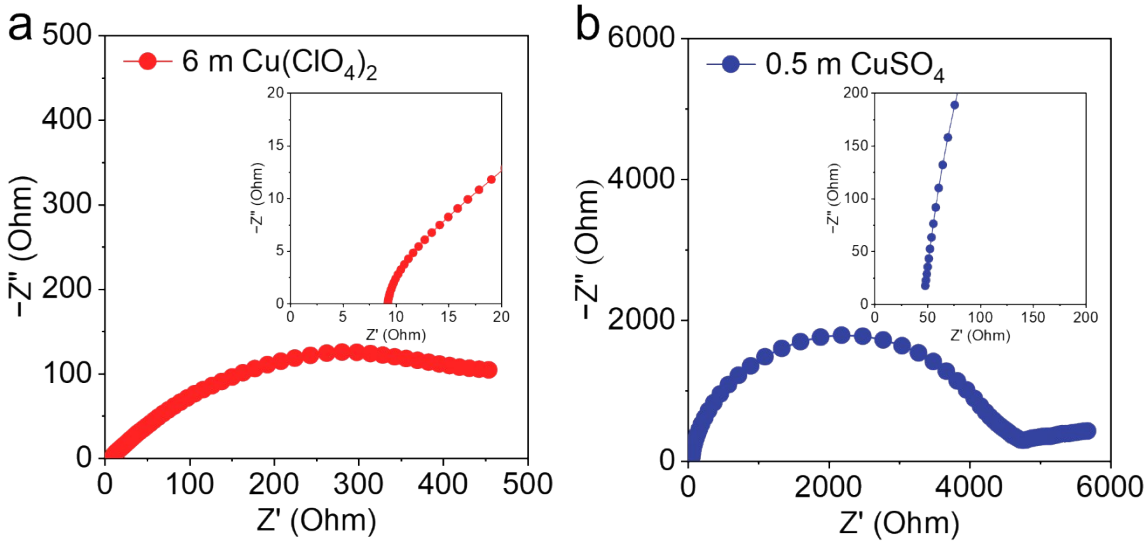

Fig. S26. Nyquist plot of EIS for (a) 6 m $Cu(ClO_4)_2$ electrolyte and (b) 0.5 m $CuSO_4$ electrolyte at room temperature.

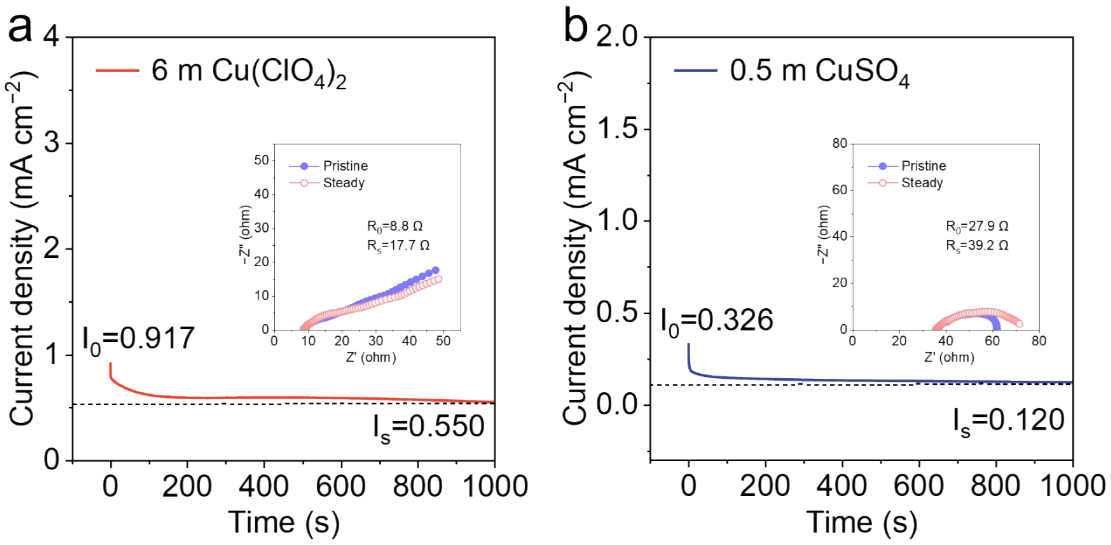

Fig. S27. Current-time curves with a constant voltage polarization of 25 mV and the insets show the impedance spectra before and after polarization. (a) 6 m $Cu(ClO_4)_2$, (b) 0.5 m $CuSO_4$.

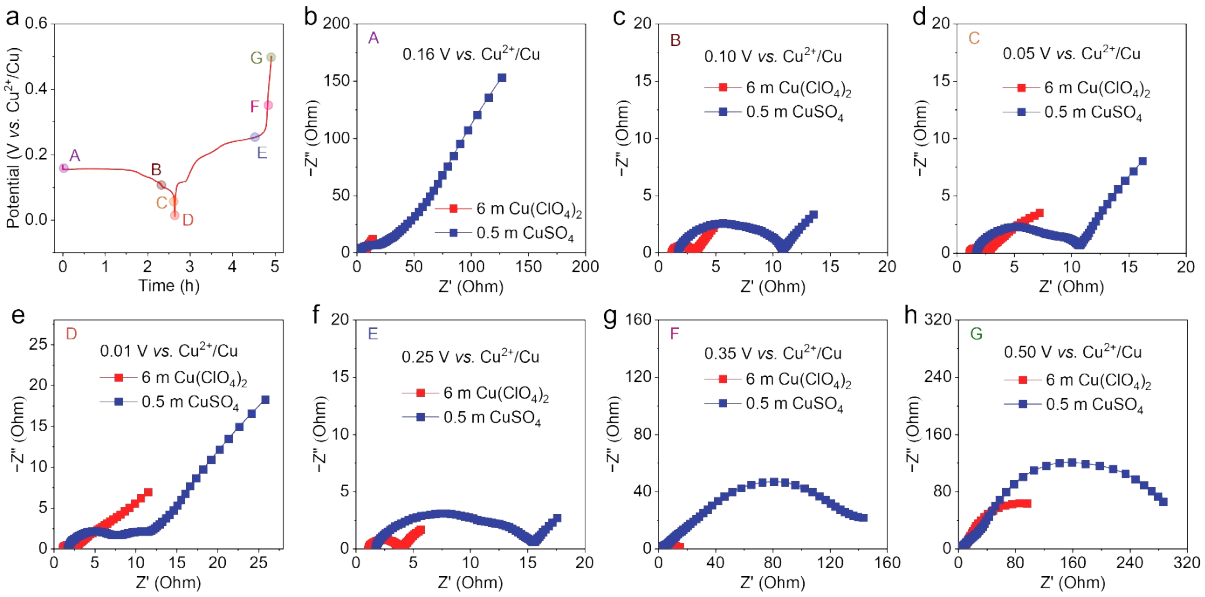

Fig. S28. (a) GCD curves for the first cycle of the Cu||Se@C cell. The comparison of EIS of the Cu|6 m $Cu(ClO_4)_2$|Se@C cells and the Cu|0.5 m $CuSO_4$|Se@C cells at different potentials, including (b) open potential (0.16 V), (c) 0.10 V, (d) 0.05 V, (e) 0.01 V, (f) 0.25 V, (g) 0.35 V, (h) 0.50 V *vs.* Cu^{2+}/Cu.

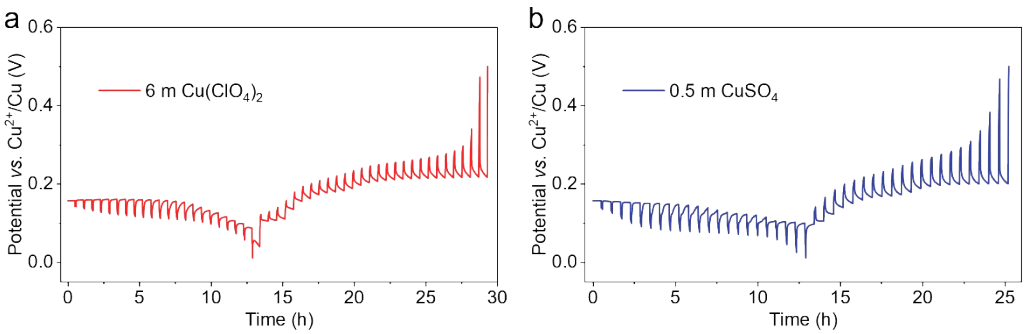

Fig. S29. The discharge/charge curves in GITT measurement of (a) the Cu|6 m $Cu(ClO_4)_2$|Se@C cell and (b) the Cu|0.5 m $CuSO_4$|Se@C cell.

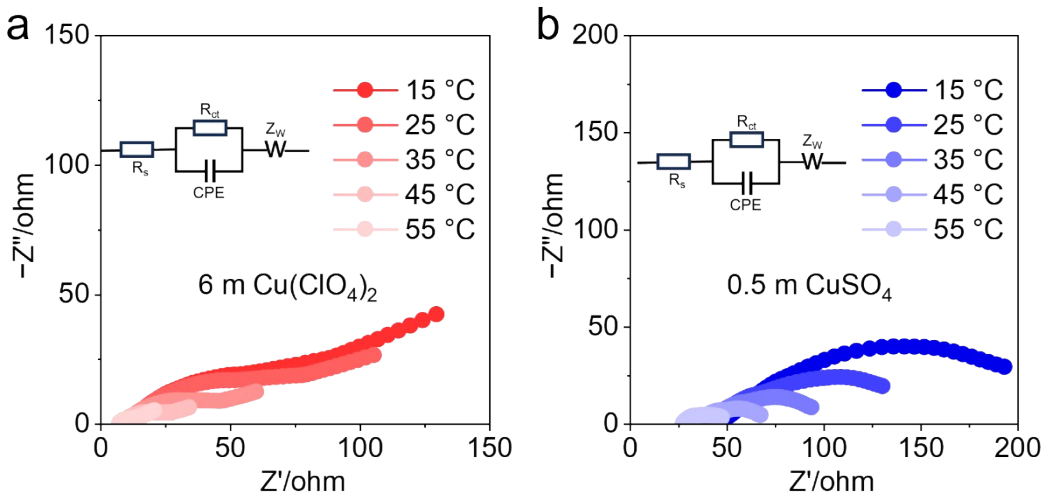

Fig. S30. The EIS of Cu||Cu symmetrical cells with (a) 6 m $Cu(ClO_4)_2$, or (b) 0.5 m $CuSO_4$ electrolytes at different temperatures and the insets show the equivalent circuit used to fit the EIS curves.

Note: In the equivalent circuit, R_s represents the intrinsic resistance, R_{ct} and the CPE in parallel with it are the charge transfer resistance and its related double-layer capacitance, and Z_W represents the Warburg impedance.

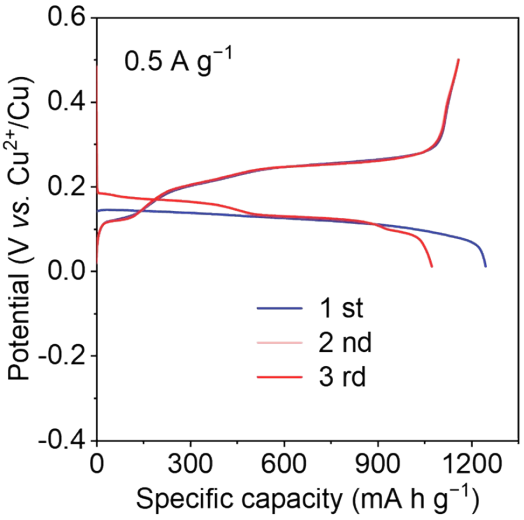

Fig. S31. GCD curves of the first three cycles of the Cu|6 m $Cu(ClO_4)_2$|Se@C cell

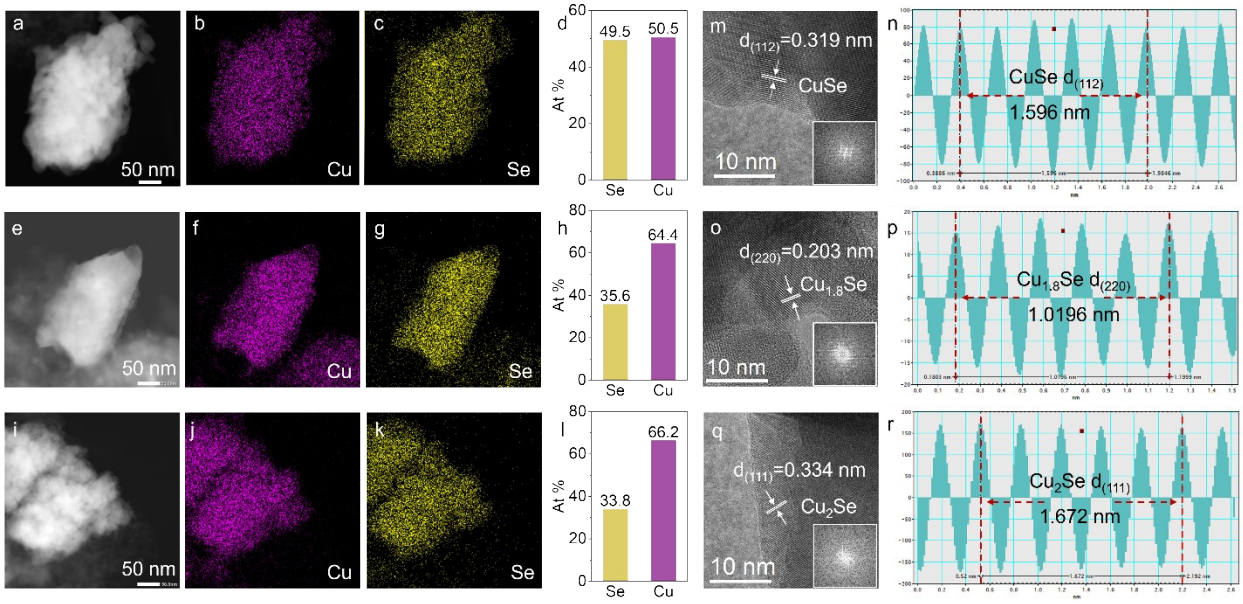

Fig. S32. TEM images, corresponding element mapping images, atomic ratio, high-resolution TEM images and lattice spacing analysis of CuSe (a-d, m, n), $Cu_{1.8}Se$ (d-h, o, p), and Cu_2Se (g-l, q, r).

The discharge products (CuSe, $Cu_{1.8}Se$, and Cu_2Se) after the three reduction peaks (corresponding to points D, E, and F in Fig. 5b) show homogeneous distribution of Se and Cu elements. As the discharge proceeds, Cu element content in the discharge products gradually increases, and the ratio of Cu to Se elements increases from 49.50 : 50.5 to 35.6 : 64.4, and finally to 33.8 : 66.2, which is basically in line with those of CuSe, $Cu_{1.8}Se$ and Cu_2Se, respectively (Fig. S32a-l). The high-resolution TEM images of the three discharge products show that their lattice spacings are 0.319, 0.203, and 0.334 nm, which coincide with the (112) plane of CuSe, the (220) plane of $Cu_{1.8}Se$, and the (111) plane of Cu_2Se, respectively (Fig. S32m-r). The ex-situ TEM proves that the discharge products after the three reduction peaks are CuSe, $Cu_{1.8}Se$ and Cu_2Se, respectively.

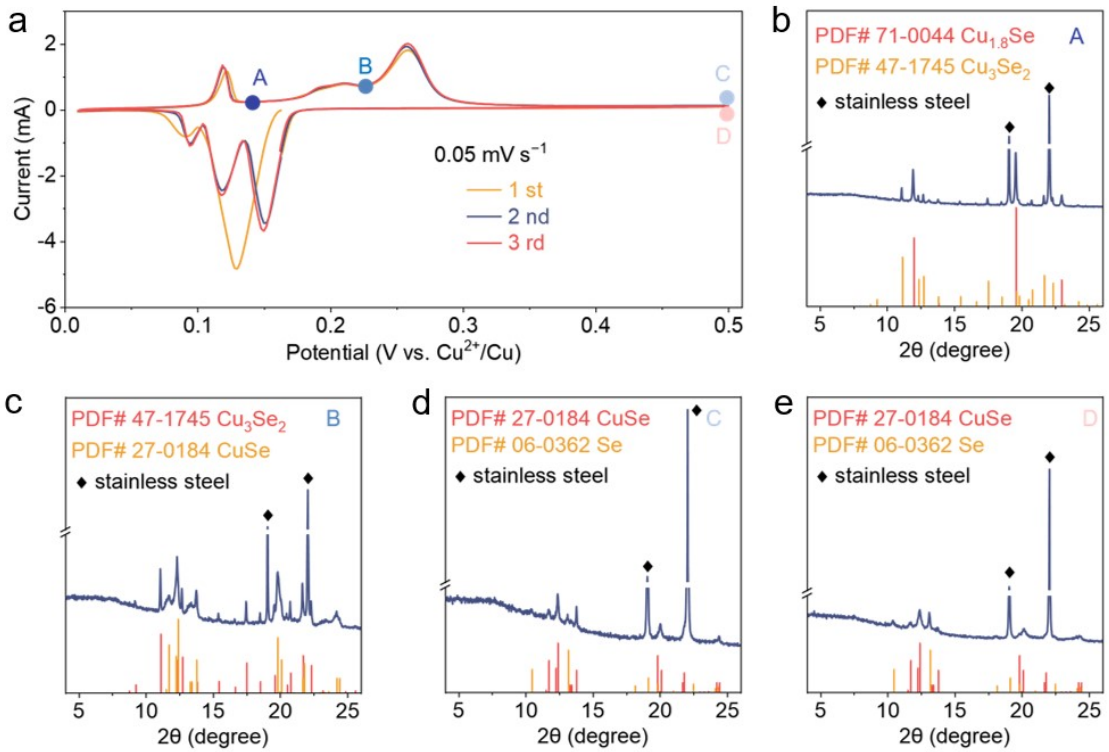

Fig. S33. (a) CV curves for the first three cycles of the Cu|6 m $Cu(ClO_4)_2$|Se@C cell. Synchrotron XRD patterns of different oxidation peaks in the (b-d) first and (e) second cycle.

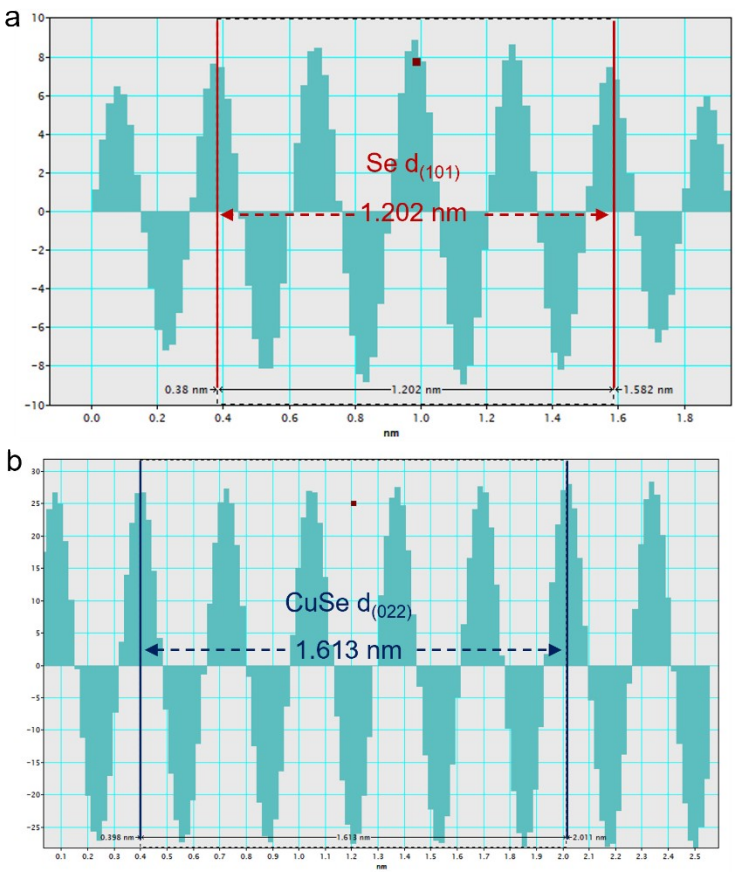

Fig. S34. Lattice spacing analysis of (a) Se and (b) CuSe.

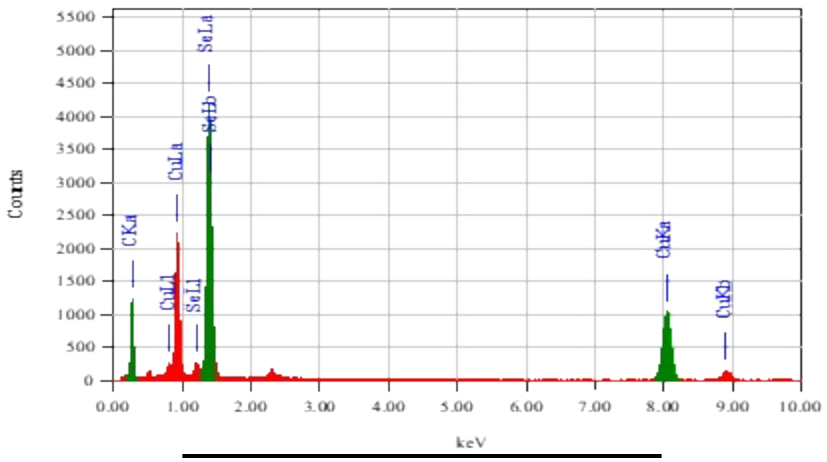

Element	Atom%
C	43.72
Cu	1.59
Se	54.69
Total	100

Fig. S35. The corresponding EDS spectrum for Fig. 5f

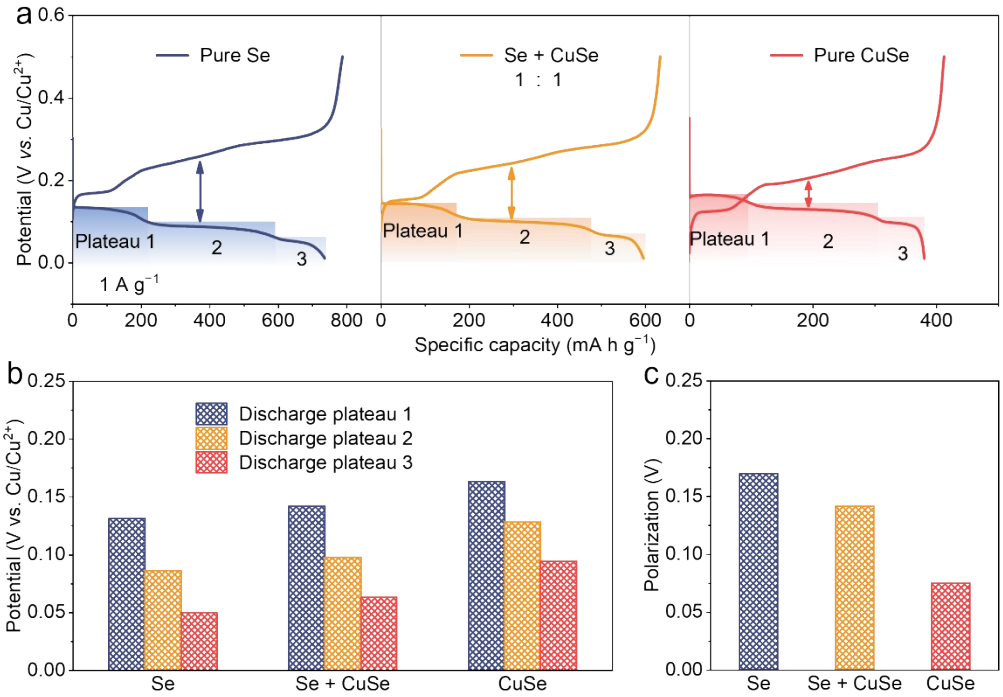

Fig. S36. GCD curves (a), comparison of three discharge plateau voltages (b) and polarization (c) of Cu||Se, Cu||(Se + CuSe) and Cu||CuSe cathodes in 6 m $Cu(ClO_4)_2$ electrolyte at 1 A g^{-1}.

Pure CuSe cathodes delivered the highest discharge plateaus and the smallest polarization voltage among them, suggesting that CuSe can accelerate the reaction kinetics and enhance its discharge voltage of the Se cathode.

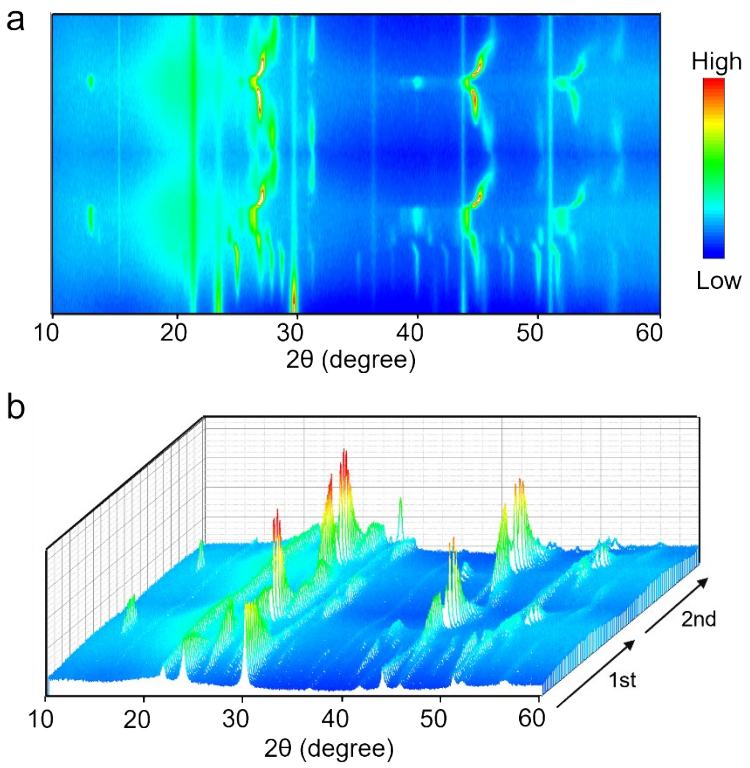

Fig. S37. Comprehensive in situ XRD patterns spanning 10° to 60° for the first two cycles.

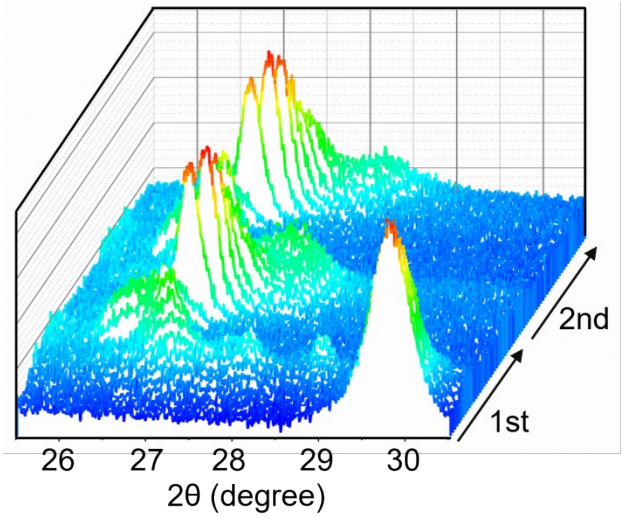

Fig. S38. In situ XRD patterns in the 25.5°~30.5° range of the cathode during the first two cycles.

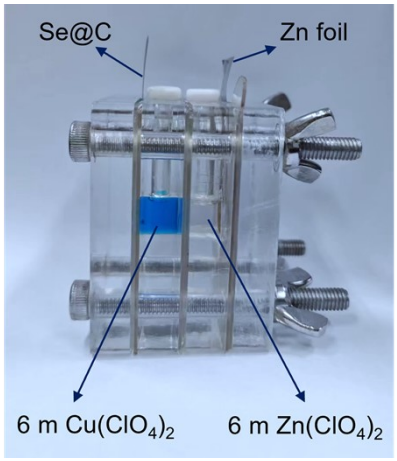

Fig. S39. The optical photograph of the homemade cell.

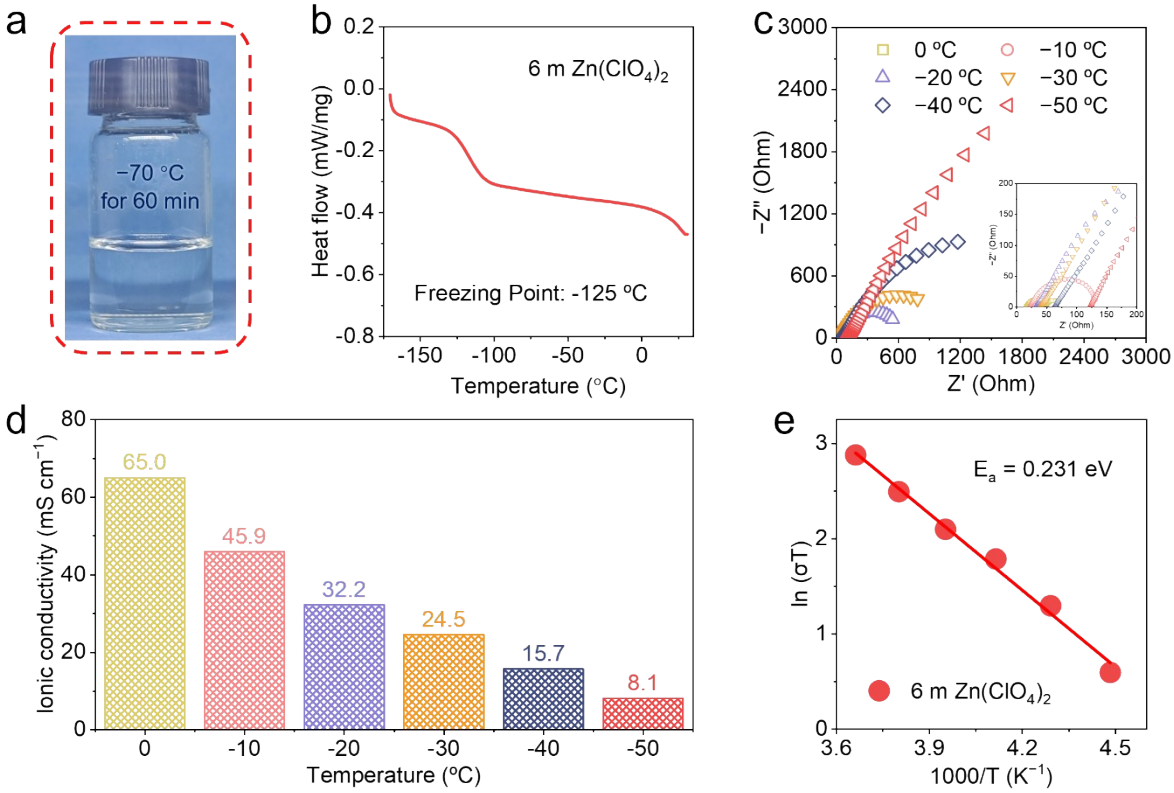

Fig. S40. (a) Optical photographs of 6 m $Zn(ClO_4)_2$ aqueous solutions at −70 °C. (b) DSC curves of 6 m $Zn(ClO_4)_2$ electrolytes. (c and d) Nyquist plot of EIS and ionic conductivities for 6 m $Zn(ClO_4)_2$ electrolytes at different temperatures. (e) The activation energies of 6 m $Zn(ClO_4)_2$ aqueous solutions within the low-temperature range of 0 to −50 °C.

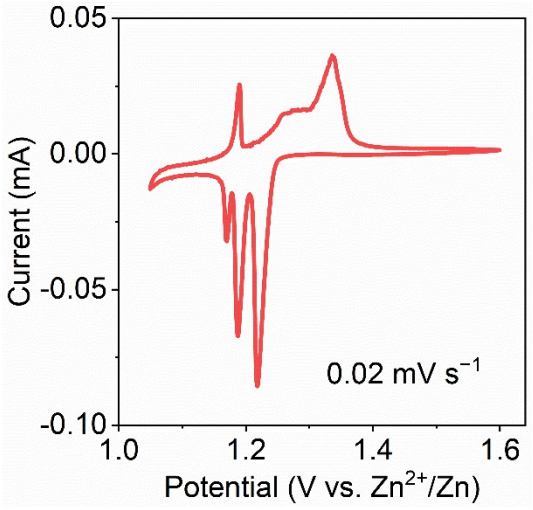

Fig. S41. CV curves of the Zn|6 m $Zn(ClO_4)_2$||6 m $Cu(ClO_4)_2$|Se@C.

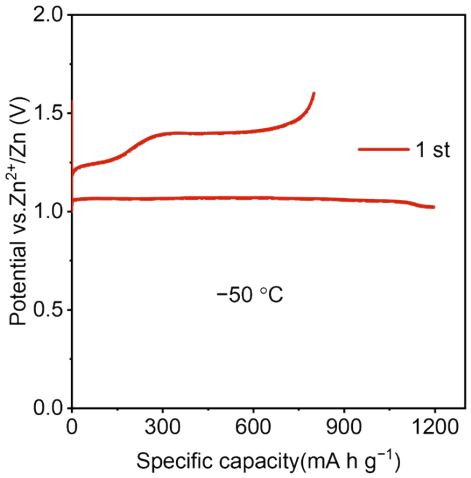

Fig. S42. The first cycle GCD curves of aqueous Zn-Se@C full cell at 0.05 A g^{-1} at −50 °C.

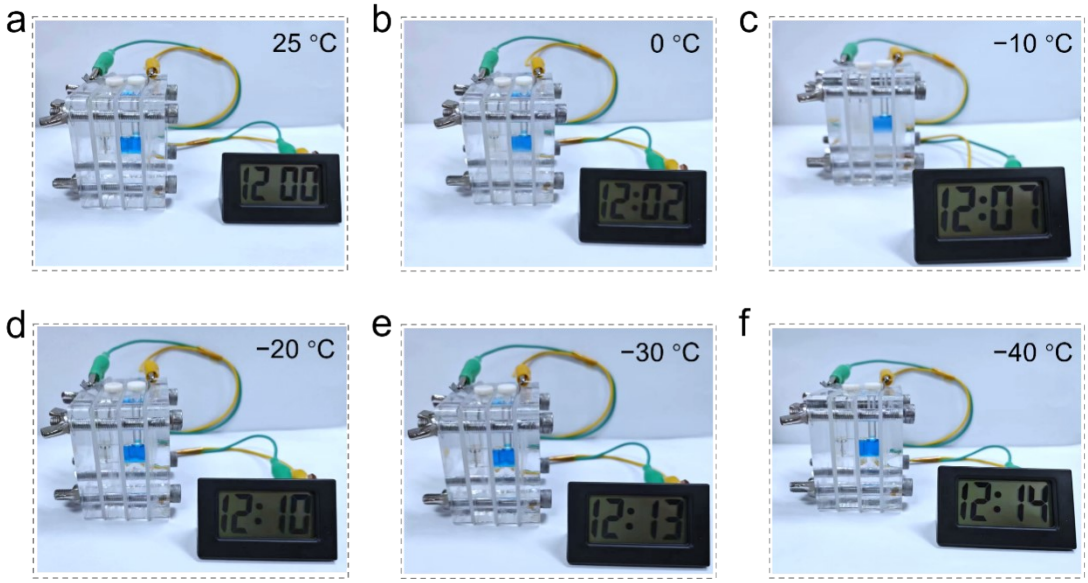

Fig. S43. The assembled Zn-Se@C full cell powers a digital watch at low temperatures of 25, 0, −10, −20, −30, and −40 °C.

Table S1. Ionic conductivities of $Cu(ClO_4)_2$ electrolytes with different concentrations at different temperatures.

Temperature (℃)	Ionic conductivity (mS cm^{-1})				
	3 m	4 m	5 m	6 m	7 m
0	68.54	75.53	81.63	102.29	86.66
−10	56.53	58.72	65.79	73.15	54.88
−20	41.43	42.55	47.57	48.45	40.62
−30	14.45	17.23	23.29	25.79	23.43
−40	5.06	8.7	11.24	12.91	8.24
−50	1.64	4.11	5.73	7.03	4.5

Table S2. The fitted R_{ct} of Cu||Cu symmetric cells with 0.5 m $CuSO_4$ and 6 m $Cu(ClO_4)_2$ electrolytes at different temperatures.

Temperature (°C)	0.5 m $CuSO_4$		6 m $Cu(ClO_4)_2$	
	R_{ct}	Error of fitted R_{ct} (%)	R_{ct}	Error of fitted R_{ct} (%)
15	190.1	1.5274	48.74	1.3976
25	116.3	1.0986	37.69	1.6101
35	63.33	0.73613	25.48	1.3623
45	37.42	0.82972	15.13	2.1273
55	22.89	1.29532	9.699	1.4728

Table S3. Electrochemical performance comparisons of low-temperature aqueous batteries.

Anode	Cathode	Electerolyte	Temperature（°C）	Discharge capacity (mA h g^{-1})/current density (A g^{-1})	Ref.
Cu	Se@C	6 m $Cu(ClO_4)_2$	−50	605 / 1 919 / 0.1	**This work**
PANI	MnO_2@CF	3.5M $Mn(ClO_4)_2$	−50	112 / 0.18	[3]
Zn	PANI	7.5 m $ZnCl_2$	−40	105 / 1	[4]
Zn	PTO	3.5 M $Mg(ClO_4)_2$ + 1 M $Zn(ClO_4)_2$	−50	120 / 0.2	[5]
ALO	CF	2 m HBF_4 + 2 m $Mn(BF_4)_2$	−30	125 / 1	[6]
Zn	PANI	2 M $Zn(ClO_4)_2$ in CSAM hydroge (CSAM-C)	−30	156 / 0.1	[7]
Zn	Ni	1 M KOH / 0.3-DMSO	−40	173 / 0.5	[8]
Zn	TCBQ	4 M $Zn(BF_4)_2$	−30	101.4 / 0.22	[9]
NTP	AC	2 M $NaClO_4$ / 0.3-DMSO	−50	65 / 0.065	[10]
Zn	α-MnO_2	3 M $Zn(ClO_4)_2$ + 0.1 M $MnSO_4$	−20	175 / 0.15	[11]
Pb	PCHL-rGO	5 M H_2SO_4	−40	119 / 0.1	[12]
Zn	PANI	5 m $Zn(ClO_4)_2$	−40	126 / 1	[13]
Zn	V_2O_5	2 M $Zn(OTf)_2$	−30	208.7 / 0.5	[14]
Zn	V_2O_5	2 M $Zn(OTf)_2$-H_2O / 2-propanol (40 vol%)	−20	175 / 1	[15]
Zn	MnO_2	2 M $ZnSO_4$ H_2O/DMSO	−20	176 / 0.1	[16]
Zn	V_2O_5	1 M $Zn(OTf)_2$ / 0.15-DME	−40	212.4 / 0.5	[17]

Table S4. The numbers of water molecules and ions in amorphous cell module (32.7 × 32.7 × 32.7 Å^3).

Electrolyte	H_2O	Cu^{2+}	ClO_4^-
H_2O	1170	—	—
3 m $Cu(ClO_4)_2$	735	30	60
4 m $Cu(ClO_4)_2$	676	34	68
5 m $Cu(ClO_4)_2$	633	37	74
6 m $Cu(ClO_4)_2$	599	39	78
7 m $Cu(ClO_4)_2$	575	41	82

References

1. H. Sun, P. Ren and J. R. Fried, *Comput. Theor. Polym. Sci.*, 1998, **8**, 229-246.
2. H. Sun, *J. Phys. Chem. B*, 1998, **102**, 7338-7364.
3. T. Sun, Q. Nian, H. Du, S. Zheng, D. Han and Z. Tao, *J. Mater. Chem. A*, 2022, **10**, 17288–17296.
4. Q. Zhang, Y. Ma, Y. Lu, L. Li, F. Wan, K. Zhang and J. Chen, *Nat. Commun.*, 2020, **11**, 4463.
5. T. Sun, S. Zheng, H. Du and Z. Tao, *Nano-Micro Lett.*, 2021, **13**, 204.
6. T. Sun, H. Du, S. Zheng, J. Shi and Z. Tao, *Adv. Funct. Mater.*, 2021, **31**, 2010127.
7. S. Huang, L. Hou, T. Li, Y. Jiao and P. Wu, *Adv. Mater.*, 2022, **34**, 2110140.
8. S. Chen, C. Peng, D. Xue, L. Ma and C. Zhi, *Angew. Chem. Int. Ed.*, 2022, **61**, e202212767.
9. T. Sun, X. Yuan, K. Wang, S. Zheng, J. Shi, Q. Zhang, W. Cai, J. Liang and Z. Tao, *J. Mater. Chem. A*, 2021, **9**, 7042–7047.
10. Q. Nian, J. Wang, S. Liu, T. Sun, S. Zheng, Y. Zhang, Z. Tao and J. Chen, *Angew. Chem. Int. Ed.*, 2019, **58**, 16994–16999.
11. G. Yang, J. Huang, X. Wan, B. Liu, Y. Zhu, J. Wang, O. Fontaine, S. Luo, P. Hiralal, Y. Guo and H. Zhou, *EcoMat.*, 2022, **4**, e12165.
12. F. Yue, Z. Tie, S. Deng, S. Wang, M. Yang and Z. Niu, *Angew. Chem. Int. Ed.*, 2021, **60**, 13882–13886.
13. M. Qiu, P. Sun, K. Han, Z. Pang, J. Du, J. Li, J. Chen, Z. L. Wang and W. Mai, *Nat. Commun.*, 2023, **14**, 601.
14. Q. Zhang, K. Xia, Y. Ma, Y. Lu, L. Li, J. Liang, S. Chou and J. Chen, *ACS Energy Lett.*, 2021, **6**, 2704–2712.
15. Q. Ma, R. Gao, Y. Liu, H. Dou, Y. Zheng, T. Or, L. Yang, Q. Li, Q. Cu, R. Feng, Z. Zhang, Y. Nie, B. Ren, D. Luo, X. Wang, A. Yu and Z. Chen, *Adv. Mater.*, 2022, **34**, 2207344.
16. D. Feng, F. Cao, L. Hou, T. Li, Y. Jiao and P. Wu, *Small*, 2021, **17**, 2103195.
17. Y. Dong, N. Zhang, Z. Wang, J. Li, Y. Ni, H. Hu and F. Cheng, *J. Energy Chem.*, 2023, **83**, 324–332.